Available online at www.sciencedirect.com

ScienceDirect

Ceramics International 40 (2014) 14983–14990

CERAMICS INTERNATIONAL

www.elsevier.com/locate/ceramint

Chemical bath deposition of IrO_2 films on ITO substrate

Jing-Yu Chen[a], Yong-Min Chen[a], Yu Sun[b], Jyh-Fu Lee[c], San-Yuan Chen[a], Po-Chun Chen[a,*], Pu-Wei Wu[a,*]

[a]Department of Materials Science and Engineering, National Chiao Tung University, Hsinchu 300, Taiwan, ROC
[b]Graduate Program for Science and Technology of Accelerator Light Source, National Chiao Tung University, Hsinchu 300, Taiwan, ROC
[c]National Synchrotron Radiation Research Center, Hsinchu 300, Taiwan, ROC

Received 13 May 2014; received in revised form 9 June 2014; accepted 18 June 2014
Available online 25 June 2014

Abstract

A chemical bath is shown to deposit an IrO_2 film on an ITO substrate. The chemical bath is prepared by mixing an Ir precursor ($Na_3IrCl_6 \cdot xH_2O$), an oxidizer (NaClO), a complexing agent ($NaNO_2$), and a complex agent/stabilizer (NaOH) in an aqueous solution at a molar ratio of 1:1.5:10:30. From the UV–vis absorption spectra, complexes such as $[Ir(OH)_6]m^{3-}$, $[Ir(NO_2)_4Cl_2]^{3-}$, and $[Ir(NO_2)_3Cl_3]^{3-}$ are identified. These complexes are relatively stable, minimizing the undesirable homogeneous precipitation of IrO_2 nanoparticles in favor of the heterogeneous growth of the IrO_2 film on the ITO substrate. Diffraction patterns from the as-deposited IrO_2 film reveal an amorphous structure. In addition, profiles from X-ray absorption spectroscopy and X-ray photoelectron spectroscopy indicate that the oxidation state of the Ir in the as-deposited IrO_2 film is +4. Thermogravimetric analysis confirms the inclusion of 10 wt% hydrated water in the as-deposited IrO_2 film. Scanning electron microscope images reveal a continuous solid film with a smooth surface. The amorphous IrO_2 film becomes rutile IrO_2 phase after a mild heat treatment in air.

Keywords: Iridium oxide; Thin film; Chemical bath deposition; Indium tin oxide

1. Introduction

The synthesis of iridium oxides has received considerable attention because iridium oxide has many unique properties that make it an ideal material for applications in electrochromism [1,2], bio-sensing [3–8], and water electrolysis [9–14]. To date, methods including thermal decomposition [15–17], sputtering deposition [13,18–20], pulsed laser deposition [21], and electrodeposition [6–9,11,22,23] have been explored for the fabrication of desirable nanoscale iridium oxide structures, such as thin films and nanoparticles. Thermal decomposition and sputtering deposition involve complex instrumentation, including heating and vacuum setups. Electrodeposition involves the use of suitable complexing agents in the plating bath to stabilize the iridium precursors (Ir^{3+} and Ir^{4+}), which are known to undergo spontaneous redox reactions triggered by photons [24]. In addition, electroplating techniques require a conductive substrate to serve as the working electrode, preventing the deposition of iridium oxide films on insulators.

An alternative solution for the synthesis is chemical bath deposition, in which the iridium precursors undergo oxidation reactions initiated by selectively incorporated oxidizers. This approach does not require externally imposed current/voltage and allows semiconducting materials to be used as the substrates for film growth [25–28]. So far, several studies have reported the formation of iridium oxide nanoparticles and investigated their electrocatalytic properties for oxygen evolution reactions in water splitting experiments [9–11,13,14,22,29–31]. However, these studies failed to describe the formation mechanisms of the iridium oxide and instead focused on material characterizations and performance evaluations. On the other hand, iridium oxide is a biocompatible electrode material which have been investigated to replace platinum to enhance the efficiency [32–34]. However, the preparation of iridium oxide traditionally uses

*Corresponding author. Tel.: +886 3 5131227; fax: +886 3 5724727.
E-mail addresses: st1019@gmail.com (P.-C. Chen), ppwu@mail.nctu.edu.tw (P.-W. Wu).

http://dx.doi.org/10.1016/j.ceramint.2014.06.098
0272-8842/

sputtering process and consumes unnecessary noble target [6,7]. In addition, aspect ratio of the substrate is limited for the sputtering process. Therefore, chemical bath deposition does not require applying voltage/current or conducting substrates, so iridium oxide film can be coated on various materials, such as Si, SiO_2, and ITO, under ambient environments. Moreover, chemical bath deposition is a relatively cost efficient process because there is no extra precursor consumed, and it has better capability to coat iridium oxide onto targeting substrate. In order to better use, it is recognized that the surface composition, structure, and morphology play critical roles in determining the resulting properties. Hence, it is necessary to better understand and have control over the fabrication process to synthesize iridium oxides with desirable properties.

In the chemical bath used to form iridium oxides, the addition of complexing agents is necessary to inhibit unwanted redox reactions among the iridium precursors. Among the explored complexing agents, the hydroxide ions are often used to facilitate the synthesis of iridium oxide nanoparticles by stabilizing the iridium ions in the form of $[Ir(OH)_6]^{2-}$; they also aid in hydrolysis and acid-catalyzed condensation, as well as precipitation reactions [12,14,23,30,35,36]. This process provides a facile route to prepare nanoparticulate iridium oxides but is ineffective for the deposition of iridium oxide thin films. Therefore, in addition to hydroxide ions, it is necessary to identify additional complexing agents to strengthen the stability of the complexed iridium ions and thus extend the lifetime of the plating bath, allowing heterogeneous precipitation to occur selectively on the intended substrates.

In this study, we demonstrate a formulation for the deposition of iridium oxide films (IrO_2) on an indium tin oxide (ITO) substrate *via* a chemical bath deposition route in which $IrCl_6^{3-}$ is used as the Ir precursor, hydroxide ions (OH^-) are used as the stabilizer and complexing agent, and nitrite ions (NO_2^-) and hypochlorite ions (ClO^-) are employed as the complexing agent and the oxidizer, respectively. The reaction steps responsible for IrO_2 formation are explored, and the material characterizations of the resulting thin films are discussed.

2. Experimental

2.1. Preparation of chemical bath

A glass slide coated with ITO (Aldrich; 8–12 Ω/sq) over an area of $2.5 \times 2.5\ cm^2$ was utilized as the substrate for the chemical bath deposition. The thickness of the ITO coating was 120–160 nm. Prior to the deposition, the ITO substrate was rinsed with deionized water and acetone to remove any debris and contaminants. The deposition bath contained 0.0474 g (1×10^{-4} mol) $Na_3IrCl_6 \cdot xH_2O$ (Aldrich), 5.5674 g (1.49×10^{-4} mol) NaClO (SHOWA), 0.12 g (3×10^{-3} mol) NaOH (Mallinchrodt), and 0.069 g (1×10^{-3} mol) $NaNO_2$ (SHOWA). The $Na_3IrCl_6 \cdot xH_2O$ and NaClO were utilized as the precursor and oxidizer, respectively. The $NaNO_2$ was used as the complexing agent for the Ir precursor. The NaOH was used both as the complexing agent for the Ir precursor and the stabilizing agent for NaClO. A schematic of the preparation of the chemical bath and the deposition process is depicted in Fig. 1. First, $Na_3IrCl_6 \cdot xH_2O$ was dissolved in deionized water, forming a pale yellow solution. Another transparent mixture was prepared by separately dissolving $NaNO_2$, NaOH, and NaClO in deionized water, and then these three solutions were mixed together. Once the Ir precursor solution was added to the transparent mixture, the resulting solution turned light yellow and was kept at 25 °C for 10 min. Subsequently, the light yellow solution was placed in a water bath at 70 °C for another 10 min, allowing the complexed Ir precursors to react with the oxidizer to form a dark blue solution. At this stage, the solution was ready for deposition, and the ITO substrate was immersed for 3 h to allow the growth of IrO_2.

2.2. Materials characterization

A UV–vis spectrometer (JASCO V-670) was used to record the absorption spectra of the deposition bath at 70 °C. A high-resolution X-ray diffractometer (XRD; Bruker D8 Discover) with a Cu *K*α radiation source of 1.54 Å was employed to identify the phase and crystallinity of the IrO_2. Thermogravimetric analysis (TGA) was employed to determine the hydration

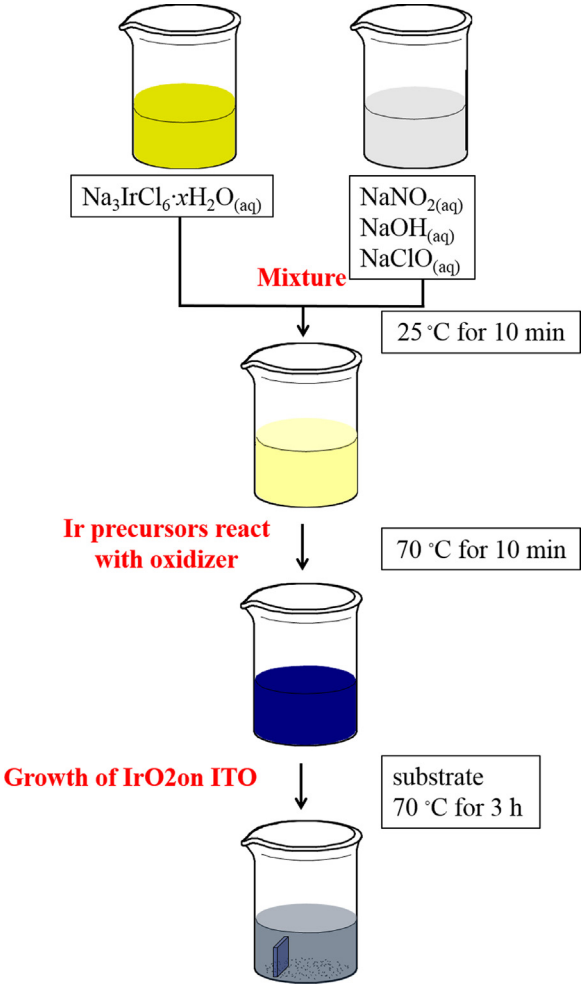

Fig. 1. An experimental flowchart of the processing steps for the IrO_2 deposition. (For interpretation of the references to color in this figure legend, the reader is referred to the web version of this article.)

state of the Ir deposit. For the TGA measurements, nitrogen (40 mL min^{-1}) and argon (60 mL min^{-1}) were used as the balance and sample gas, respectively, and the heating rate was maintained at 3 °C min^{-1}. A particle sizer (Beckman Coulter Delsa™ Nano C particle analyzer) was used to determine the ζ-potential of the suspended nanoparticles in the bath. An X-ray photoelectron spectrometer (XPS; Thermo Microlab 350) with an Mg target was used to identify the oxidation state of the Ir deposits. Prior to the XPS measurements, additional Pt was sputtered onto the IrO_2 surface to supply a correction standard for the binding energy of Pt $4f_{7/2}$. The film surface was bombarded with Ar ions at 3 kV and 1 μA for 30 s prior to recording the XPS signals. A field-emission scanning electron microscope (FE-SEM; JEOL-JSM-6500F) with a 15 keV operating voltage was used to observe the morphology and thickness of the deposited film.

X-ray absorption spectroscopy (XAS) of the Ir L_{III}-edge was used to determine the chemical nature of the Ir in both the deposition bath and the deposited film. The XAS spectra were obtained from the BL17C1 and BL01C1 beam lines at the National Synchrotron Radiation Research Center at Hsinchu, Taiwan, and the standard operating conditions were 1.5 GeV and 300–360 mA. The photon energy was calibrated using the L_{III}-edge of a metallic Ir foil, and the XAS data were recorded in a fluorescence mode at 25 °C in air. A Zn foil was utilized as a fluorescence filter for the photons entering the fluorescence detector. The resulting spectra were processed by a program (Athena, version 0.8.056) in which the Ir L_{III}-edge absorption steps were normalized to unity with removal of the background signals. Because the film was deposited on an ITO substrate, no reference signal was collected from the reference chamber. Therefore, the self-prepared Ir and IrO_2 films were used as the standards for the X-ray absorption near-edge structure (XANES). These self-prepared standards were fabricated using identical deposition time and formulation, but the as-deposited films were subjected to additional heat treatments in hydrogen (30%H_2/70%Ar for 30 min) and air (30 min), respectively. The detailed XAS experimentation and analysis process has been reported elsewhere [37].

3. Results and discussion

We performed the chemical bath deposition at 70 °C to accelerate the deposition rate; at 25 °C, the light yellow solution required at least 48 h to transition to dark blue and become ready for deposition. Notably, once the solution appeared dark blue in color, colloids of IrO_2 were deposited heterogeneously only onto the ITO substrate. There was no IrO_2 coated onto SiO_2 side of the substrate because there was a very slow etching of SiO_2 in alkaline solution. In addition, IrO_2 was precipitated homogeneously throughout the solution. The presence of both homogeneous and heterogeneous precipitates was not unexpected because similar phenomena have been reported in previous studies [12,36,38]. Because the bath at 70 °C was relatively unstable, neither sensitization nor activation of the ITO substrate was required, simplifying the deposition process and reducing the likelihood of contamination.

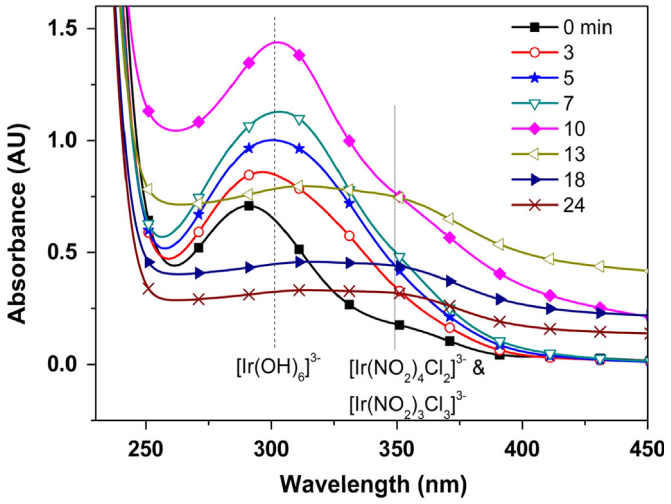

Fig. 2. UV–vis spectra from the IrO_2 deposition bath at 70 °C as a function of time. The deposition bath contained $Na_3IrCl_6 \cdot xH_2O$, NaClO, NaOH, and $NaNO_2$. (For interpretation of the references to color in this figure legend, the reader is referred to the web version of this article.)

Fig. 2 displays the in-situ UV–vis spectra of the deposition bath at 70 °C. From 0 to 10 min, a broad absorption peak located at approximately 300 nm and a minor peak at 350 nm were observed, and their intensities increased progressively with time. At this stage, the color of the deposition bath was light yellow. The absorption peak at 300 nm was attributed to $[Ir(OH)_6]^{3-}$, and the minor absorption peak at 350 nm was associated with $[Ir(NO_2)_4Cl_2]^{3-}$ and $[Ir(NO_2)_3Cl_3]^{3-}$. The assignments of these absorption peaks show that these complexes were the most kinetically stable complexes of Ir in similar formulations. After 10 min at 70 °C, we observed the formation of precipitates in conjunction with a decrease in the absorption peak at 300 nm. This observation indicates that the concentration of $[Ir(OH)_6]^{3-}$ decreased continuously upon precipitation. In addition, the precipitate formation produced a notable increase in the absorption intensities for the wavelengths below 250 nm. These increases were due to the scattering effect of the suspended precipitates. Table 1 summarizes the results from a literature survey of the UV–vis absorption peaks observed from various Ir precursors in solution. Importantly, the increase and decline of the 300 nm absorption peak in Fig. 2 suggests the complexation of Ir^{3+} by OH^- ligands and their subsequent removal to form IrO_2. In contrast, the absorption peak at approximately 350 nm experienced only a subtle change in intensity, suggesting that the NO_2^- ligands formed stronger Ir complexes. We believed that the OH^- ligands were more easily oxidized by the NaClO to produce IrO_2 than the NO_2^- ligands because the reduction of the absorption peak at 350 nm was moderate compared with that at 300 nm.

Once the precipitation process began, the overall background absorption intensity increased steadily due to the scattering of the dark blue nanoparticles. To verify the role of the OH^- ligands in the deposition bath, we prepared a solution containing the Ir precursors, OH^-, and NaClO, and studied its absorption profile as a function of time (Fig. 3). In

Table 1
Literature survey of iridium species and their characteristic UV–vis absorption peaks and colors.

Ir oxidation state	Species	UV–vis absorption (nm)	Color	References
3+	$[IrCl_6]^{3-}_{(aq)}$	358, 414	Yellow	[30,39]
	$[Ir(OH)_6]^{3-}_{(aq)}$	312	Yellow	[30,39]
	$[(H_2O)_4Ir(OH)_2Ir(H_2O)_4]^{4+}_{(aq)}$	318	Yellow	[38,39]
	$[Ir(H_2O)_6]^{3+}_{(aq)}$	267 & 313	Pale yellow	[38]
	$[(H_2O)_5Ir(OH)Ir(H_2O)_5]^{5+}_{(aq)}$	265 & 310	N/A	[38]
	$Ir(OH)_3(H_2O)_{3(s)}$	N/A	Colorless	[39]
	$Ir_2O_{3(s)}$	N/A	Pale green	[39]
4+	$Ir^{4+}_{(aq)}$	547	Purple or blue	[40]
	$[IrCl_6]^{2-}_{(aq)}$	303, 420, 487	Red brown	[30,39]
	$[Ir(OH)_6]^{2-}_{(aq)}$	313	Yellow	[12]
	$IrO_2 \cdot 2H_2O_{(s)}$	N/A	Dark blue	[39]
	$IrO_{2(s)}$	N/A	Black	[39]
5+	$Ir^{5+}_{(aq)}$	447 & 640	Brown green	[38]

the absence of $NaNO_2$, we could better elucidate the hydrolysis and condensation process of the Ir precursors. Upon the formation of $[Ir(OH)_6]^{3-}$, a minor absorption peak at 570 nm appeared, in addition to the strong absorption peak at 300 nm. Over the past two decades, numerous studies have suggested that the absorption peak at 570–590 nm arises due to the formation of IrO_2 colloids [22,36,39]. However, we believe that Ir dimer complexes or oligomers may also contribute to this peak because they are readily produced in aqueous solutions [29]. Recent studies have also indicated that these Ir complexes can exist as dimers or oligomers, and act as intermediates prior to the formation of IrO_2 [29,38,40].

Fig. 4 depicts the XANES spectra for the Ir L_{III}-edge from the as-deposited film and the Ir precursor solutions at 25 °C prior to the formation of the colloidal nanoparticles. For the XAS L-edge absorption profiles, the magnitude of the absorption intensity indicates the available vacant states in the d-orbitals, and its magnitude is therefore proportional to the oxidation state of the absorbing atoms [41]. Fig. 4(a) provides the XANES spectra and Fig. 4(b) shows an enlargement of spectra. The absorption profile of the aqueous Ir precursor solution ($Na_3IrCl_6 \cdot xH_2O$; labeled as (i) in the legend) served as the standard for Ir^{3+}. The XAS signals from the as-deposited film (labeled as (ii) in the legend) and the self-prepared IrO_2 (labeled as (iii) in the legend) exhibited a strong resemblance, suggesting that the oxidation state of Ir in the as-deposited film was Ir^{4+}. Interestingly, the reflection points for the as-deposited film (11,216.4 eV) and self-prepared IrO_2 (11,216 eV) were rather close. We also prepared solutions of $NaNO_2$, NaOH, and NaClO (labeled as (iv), (v), and (vi) in the legend) and determined that the oxidation states of the Ir contained in them were between Ir^{3+} and Ir^{4+}. During the data collection for the XAS spectra, minor precipitation of IrO_2 may have occurred, even at 25 °C. Therefore, it was expected that these solutions simultaneously contained Ir complexes (Ir^{3+}) and IrO_2 nanoparticles (Ir^{4+}), rendering an averaged Ir oxidation state between Ir^{3+} and Ir^{4+}. Solution (iv) contained the iridium precursors and $NaNO_2$ but lacked OH^- and was pale yellow in color. The pale yellow solution, with a pH of 4.04, remained stable for over a month at 25 °C. This result suggests that the Ir

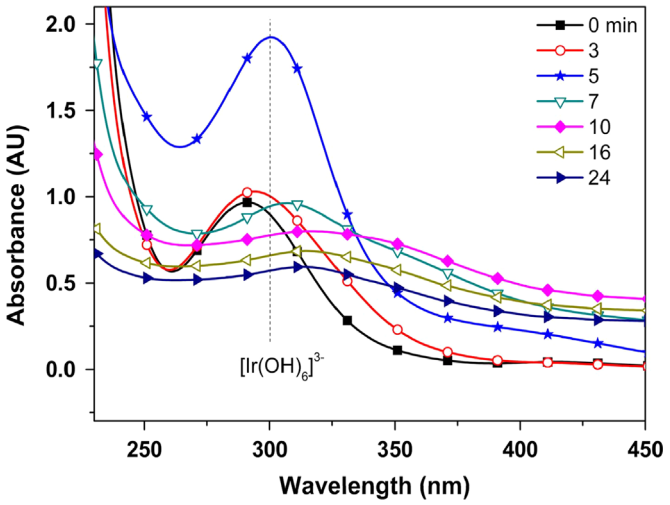

Fig. 3. UV–vis spectra from the reference bath at 70 °C as a function of time. The reference bath contained $Na_3IrCl_6 \cdot xH_2O$, NaClO, and NaOH.

complexes with the NO_2^- ligands and forms a very stable complex in aqueous solution, with subdued heterogeneous nucleation and growth. In contrast, solution (v), which consisted of the iridium precursor, NaClO, and NaOH, was able to deposit IrO_2 on the substrate. However, in this formulation, rapid homogeneous precipitation led to the notable appearance of suspended nanoparticles. Solution (vi) displayed a moderate Ir oxidation state, indicating that the solution contained stable NO_2^--coordinated complexes and IrO_2 colloids. It has been reported that nitrite ions (NO_2^-) are able to replace Cl^- ligands to form nitroiridate complexes in aqueous solution, with the most kinetically stable ions being *trans*-$[Ir(NO_2)_4Cl_2]^{3-}$ and *fac*-$[Ir(NO_2)_3Cl_3]^{3-}$. This result suggests that the presence of NO_2^- complexes inhibited the rapid IrO_2 colloid formation. In short, based on our observations, the introduction of OH^- and NO_2^- ligands into the Ir precursor solution markedly improved the lifetime of the resulting deposition bath and significantly reduced homogeneous precipitation.

In our formulation, the molar ratio of $Na_3IrCl_6 \cdot xH_2O$:NaClO:NaOH:$NaNO_2$ was 1:1.5:30:10. As mentioned in the

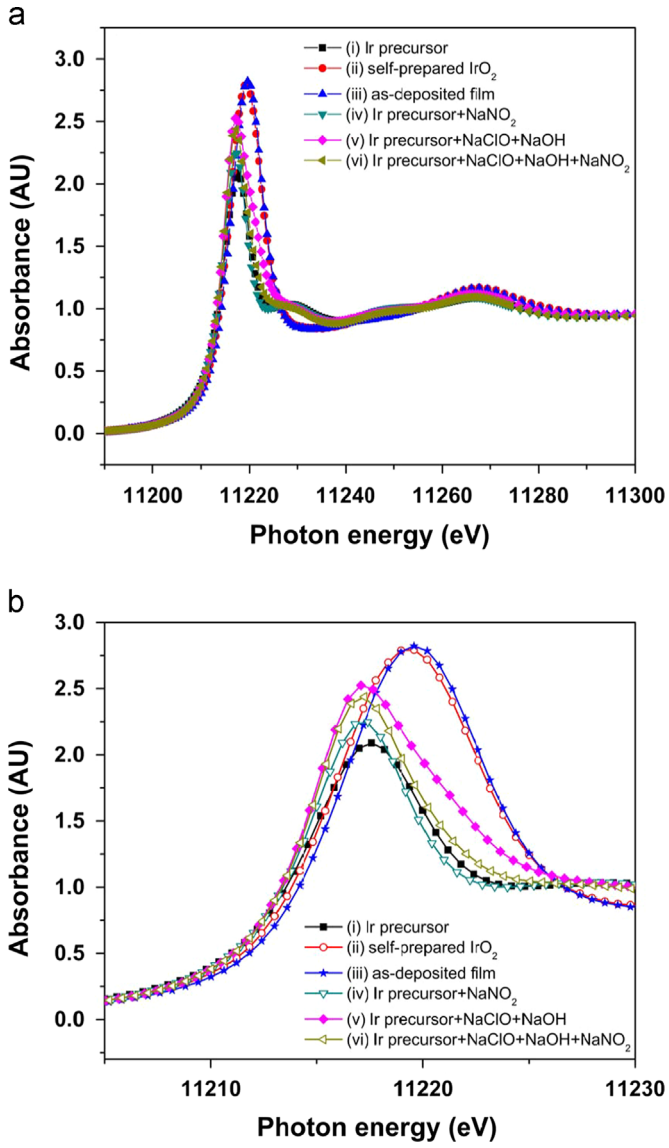

Fig. 4. The XANES spectra for the Ir L_{III}-edge from the as-deposited film and the Ir precursor solutions at 25 °C prior to the formation of the colloidal nanoparticles. (a) Ir L_{III}-edge XANES spectra of (i) Na_3IrCl_6 aqueous solution; (ii) self-prepared IrO_2; (iii) the as-deposited IrO_2 film; (iv) aqueous solution of Na_3IrCl_6 and $NaNO_2$; (v) aqueous solution of Na_3IrCl_6, $NaNO_2$, and NaOH; and (vi) aqueous solution of Na_3IrCl_6, $NaNO_2$, NaOH, and NaClO (the IrO_2 plating bath). (b) spectra enlargement of (a). The profiles were recorded at 25 °C prior to the formation of colloidal precipitates. The self-prepared IrO_2 was obtained by subjecting the as-deposited IrO_2 film to thermal annealing in ambient atmosphere for 30 min. The resulting XRD pattern confirmed the formation of crystalline IrO_2.

experimental section, to prepare the deposition bath, all chemicals except the Ir precursors were mixed together in deionized water at 25 °C. Once the Ir precursors were added, the NO_2^- ions coordinated to the Ir ions, replacing the Cl^- ligands and resulting in the formation of nitroiridate(III) ions. It has been reported that $[Ir(NO_2)_4Cl_2]^{3-}$ and $[Ir(NO_2)_3Cl_3]^{3-}$ are the most kinetically-stable species among the nitroiridate (III) ions, as listed in Eq. (1) below. As the temperature of the deposition bath was increased to 70 °C, due to the presence of OH^- and the elevated temperature, ligand exchange occurred, leading to a predominance of pale yellow $[Ir(OH)_6]^{3-}$ ions and a minor presence of dark blue Ir oligomers, as listed in Eq. (2) below. It is recognized that the Ir oligomers might undergo hydrolysis reactions to produce IrO_2, as listed in Eq. (6). However, we believed that the extent of the hydrolysis reactions from the Ir oligomers was relatively minor because of the slow formation rate of the oligomers, as discussed in Fig. 3 (relative to the rate of formation of the predominant $[Ir(OH)_6]^{3-}$). Due to the presence of a strong oxidizing agent (hypochlorite ions), the ClO^- oxidized the Ir^{3+} complexes, including $[Ir(OH)_6]^{3-}$, $[Ir(NO_2)_4Cl_2]^{3-}$, and $[Ir(NO_2)_4Cl_2]^{3-}$, producing iridium oxide, as outlined in Eqs. (3)–(5), respectively. The iridium oxides produced from these deposition reactions contained oxygen defects, making the expected chemical formula IrO_2. Eq. (3) was expected to proceed faster than Eq. (4) and Eq. (5). In the control solution, which did not contain NO_2^- (contained the Ir precursor, NaOH, and NaClO only), we observed the steady formation of bubbles in the solution, which were most likely $Cl_{2(g)}$. This Cl_2 formation was attributed to the relatively slow reaction rates of Eq. (4) and Eq. (5) compared with the stronger and more rapid NO_2^- coordination to the Ir centers. In addition, among the proposed equations, Eq. (2) and Eq. (3) are the most kinetically favorable due to the facile complexing ability of the OH^- ligands. Between NO_2^- and OH^-, the former exhibits a stronger electron affinity, which resulted in greater electron transfer from the Ir ions and the stable coordination between the NO_2^- ligands and the Ir ions. The overall reaction route is depicted in Fig. 5.

$$2[IrCl_6]^{3-}_{(aq)} + 7NO^{2-}_{2(aq)} \rightarrow [Ir(NO_2)_4Cl_2]^{3-}_{(aq)} + [Ir(NO_2)_3Cl_3]^{3-}_{(aq)} + 7Cl^-_{(aq)} \quad (1)$$

$$IrCl^{3-}_{6(aq)} + 6OH^-_{(aq)} \rightarrow [Ir(OH)_6]^{3-}_{(aq)} + 6Cl^-_{(aq)} + \text{oligomer} \quad (2)$$

$$2ClO^-_{(aq)} + 2[Ir(OH)_6]^{3-}_{(aq)} \rightarrow Cl_{2(g)} + 2IrO_{2(s)} + 8OH^-_{(aq)} + 2H_2O_{(l)} \quad (3)$$

$$2ClO^-_{(aq)} + 2[Ir(NO_2)_4Cl_2]^{3-}_{(aq)} + 4OH^-_{(aq)} \rightarrow Cl_{2(g)} + 2IrO_{2(s)} + 4Cl^-_{(aq)} + 8NO^-_{2(aq)} + 2H_2O_{(l)} \quad (4)$$

$$2ClO^-_{(aq)} + 2[Ir(NO_2)_3Cl_3]^{3-}_{(aq)} + 4OH^-_{(aq)} \rightarrow Cl_{2(g)} + 2IrO_{2(s)} + 6Cl^-_{(aq)} + 6NO^-_{2(aq)} + 2H_2O_{(l)} \quad (5)$$

$$\text{oligomer} \rightarrow IrO_{2(s)} \quad (6)$$

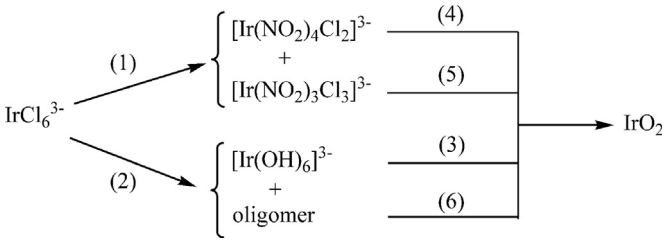

Fig. 5. A schematic of the reaction paths involved in the deposition of the IrO_2 film.

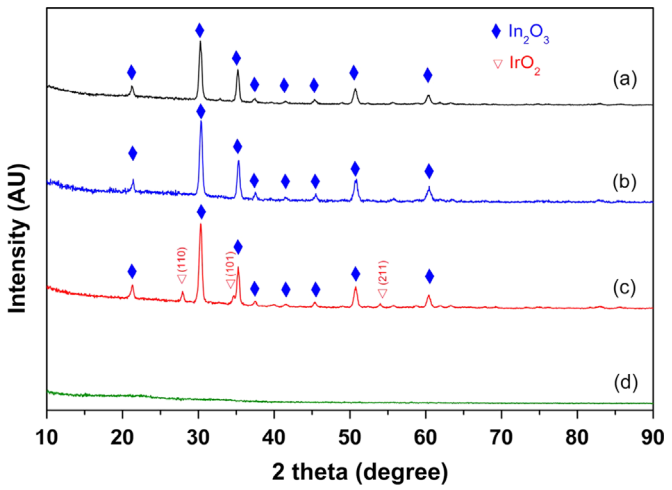

Fig. 6. The XRD patterns of (a) as-deposited IrO_2 film, (b) ITO substrate, (c) heat-treated IrO_2 film, and (d) suspended precipitates filtered from the plating bath.

Fig. 6 provides the XRD patterns of the as-deposited film, the ITO substrate, the heat-treated IrO_2 film, and the suspended precipitates filtered from the plating bath. The patterns of the as-deposited film and the ITO substrate exhibited a remarkable similarity, suggesting that the diffraction peaks of the as-deposited film resulted entirely from the ITO substrate (cubic In_2O_3, JCPDS 01-071-2194). In addition, compared with the standard IrO_2 pattern (JCPDS 00-043-1019), none of the characteristic diffraction peaks associated with rutile IrO_2 were observed. The crystallinity of the IrO_2 film was further improved simply by subjecting the as-deposited film in a heat treatment at 500 °C for 30 min in air. The as-deposited film was amorphous but after the heat treatment, the IrO_2 became a crystalline rutile phase (shown in Fig. 6(c)). The grain size estimated from Scherrer's equation for the rutile IrO_2 (1 1 0) phase at 27.9 ° is 18.47 nm. Therefore, we concluded that the as-deposited film was amorphous in nature. The pattern from the suspended precipitates exhibited no apparent diffraction peaks, as shown in Fig. 6(d). This result suggested that the suspended precipitates were amorphous IrO_2. The suspended precipitates underwent further zeta potential measurements, revealing a ζ-potential of 3.86 ± 4.97 mV. This low ζ-potential value indicates relatively weak repulsive forces among the colloids, which led to moderate aggregation and a more rapid deposition rate following the initial nucleation stage. Notably, the deposited sample contained hydrated H_2O, and according to TGA analysis, a weight loss of 10% occurred under 200 °C. This 10% weight loss was attributed to the hydrated H_2O in the amorphous IrO_2 film.

Fig. 7 displays the XPS profiles of Ir 4f and O 1s. The signals from commercial iridium materials such as Ir, IrO_2, and $IrO_2 \cdot xH_2O$ were utilized as the standards for the spectra. As depicted in Fig. 7(a), the binding energy of Ir was located at 63.41 and 60.44 eV for Ir $4f_{5/2}$ and $4f_{7/2}$, respectively. Fig. 7(b) reveals that the binding energy of O 1s was positioned at 530.4 eV. Table 2 provides the binding energy of Ir and O for the standards and the as-deposited sample.

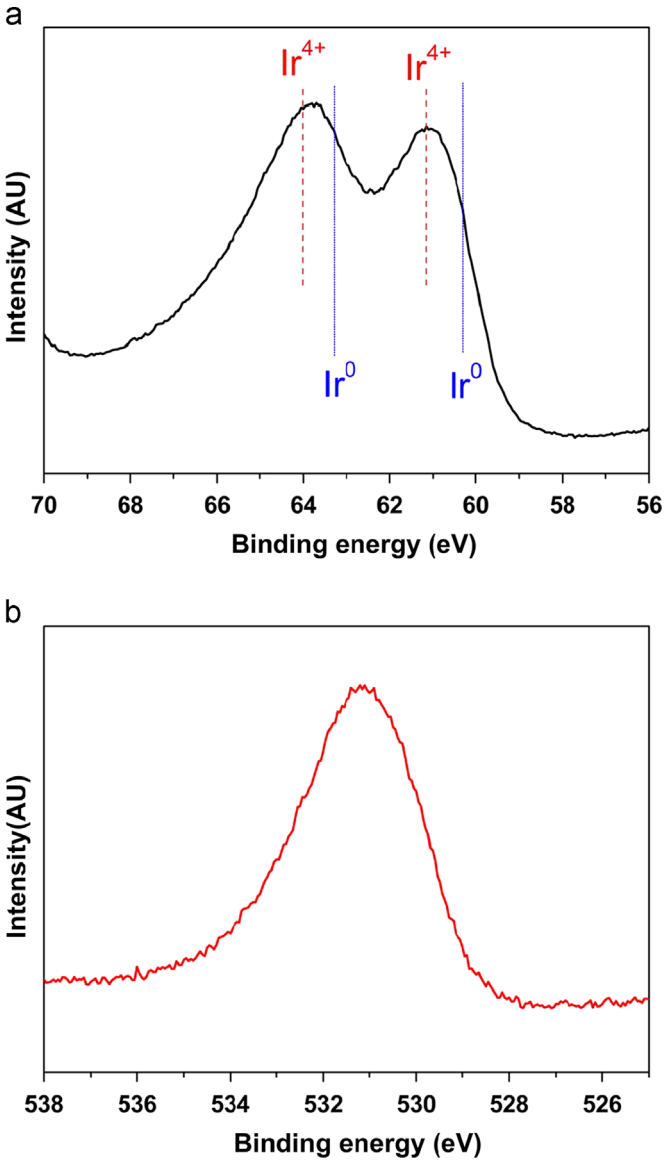

Fig. 7. XPS signals from the as-deposited IrO_2 film for (a) Ir 4f and (b) O 1s.

Through comparison with the signals from the commercial metallic iridium and iridium oxides, it is apparent that the oxidation state of Ir in the as-deposited film was approximately Ir^{4+}. Because the doublet signals ($4f_{5/2}$ and $4f_{7/2}$) from Ir were close in value, the curve fit to the iridium 4f level for composition determination exhibited substantial uncertainty. Table 2 also lists the oxygen signals from the standards and the as-deposited film, which suggest that the as-deposited film was close in oxidation state to IrO_2. The XPS profile from the $IrO_2 \cdot nH_2O$ standard contained oxygen signals from both metal oxides and hydrated water. This result confirms that the oxygen in the as-deposited film was correctly assigned to the oxygen atoms in the metal oxides rather than the oxygen atoms in the hydrated water. That is to say, the as-deposited film contained less hydrated water than commercial $IrO_2 \cdot nH_2O$. This finding is consistent with the TGA result discussed above.

Table 2
Binding energies of Ir and O as determined by XPS.

		Ir		O
		$4f_{5/2}$ (eV)	$4f_{7/2}$ (eV)	1s (eV)
Standards	Ir	63.32	60.30	531.73
	IrO_2	63.88	61.14	530.10
	$IrO_2 \cdot nH_2O$	63.67	61.21	531.42
Sample	As-deposited film	63.41	60.44	530.40

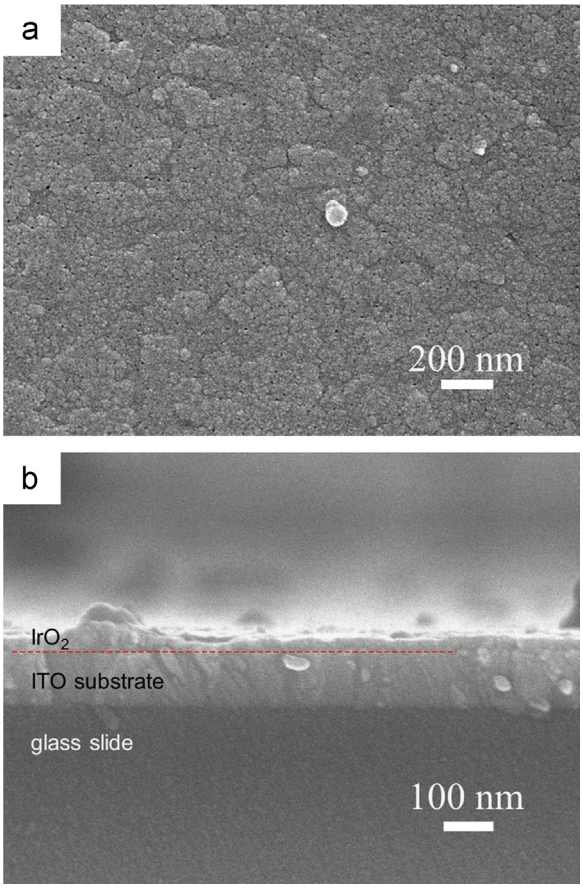

Fig. 8. FE-SEM images of the as-deposited IrO_2 film on an ITO substrate in (a) planar and (b) cross-sectional views.

Fig. 8 presents the FE-SEM images of the as-deposited IrO_2 films on an ITO substrate in planar and cross-sectional views. The surface morphology was relatively smooth, as shown in Fig. 8(a), and measurements from atomic force microscopy determined an average roughness of 3.55 nm. It can be observed that the film was possibly formed by the coalescence of individual nanoparticles into larger islands. In the cross-sectional view which is shown in Fig. 8(b), the average film thickness was only 39 nm. The as-deposited film was found to be continuous, as pinholes and voids were not observed. The film quality of the as-deposited film in our work is similar to those reported in the literatures. For example, Cruz et al. employed an electrodeposition process to deposit amorphous IrO_x on a Pt-coated glass, and the as-deposited film revealed a granular morphology [5]. In addition, Zhao et al. electroplated a colloidal IrO_x film on a fluorine-doped tin oxide substrate and observed a granular morphology on the surface [22]. In addition, Steegstra and Ahlberg demonstrated identical granular surface from the electroplated IrO_2 on a gold substrate [29]. It seems that the granular microstructure is rather common for IrO_x film derived from the electrochemical route. It is also noted that after the minor heat treatment in air, the morphology for the crystalline rutile IrO_2 film was similar to the as-deposited amorphous film.

4. Conclusions

We developed a formulation to deposit IrO_2 films on an ITO substrate. The deposition bath contained aqueous solution of $Na_3IrCl_6 \cdot xH_2O$, $NaNO_2$, NaClO, and NaOH. From the UV–vis absorption spectra, we identified the presence of $[Ir(OH)_6]^{x3-}$, $[Ir(NO_2)_4Cl_2]^{3-}$, and $[Ir(NO_2)_3Cl_3]^{3-}$ in the deposition bath. These complexes enabled an improved lifetime by minimizing homogeneous precipitation in favor of the heterogeneous growth of the IrO_2 film. The XRD patterns from the as-deposited IrO_2 film revealed an amorphous structure but a crystalline rutile IrO_2 film was formed after a mild heat treatment. In addition, the XAS and XPS results suggested the oxidation state of the Ir in the as-deposited film was Ir^{4+}. TGA analysis confirmed the inclusion of 10 wt% hydrated water in the as-deposited IrO_2 film. SEM images demonstrated a continuous solid film with moderate surface roughness. According to this study, more applications of IrO_2 can be investigated by coating it on various kind/ shape of substrates, such as TiO_2 and Al_2O_3 microprobes, via this chemical bath deposition method [6,7,31,42].

Acknowledgements

The financial supports from the National Science Council (NSC100-2221-E009-075-MY3; 103-3113-P-008-001) and the Biomedical Electronics Translational Research Center (BETRC) of National Chiao Tung University are greatly appreciated.

References

[1] M.A. Petit, V. Plichon, Anodic electrodeposition of iridium oxide films, J. Electroanal. Chem. 444 (2) (1998) 247–252.

[2] Y. Mo, I.C. Stefan, W.-B. Cai, J. Dong, P. Carey, D.A. Scherson, In situ iridium L_{III}-edge X-ray absorption and surface enhanced Raman spectroscopy of electrodeposited iridium oxide films in aqueous electrolytes, J. Phys. Chem. B 106 (14) (2002) 3681–3686.
[3] M. Rodriguez, G. Rivas, An enzymatic glucose biosensor based on the codeposition of rhodium, iridium, and glucose oxidase onto a glassy carbon transducer, Anal. Lett. 34 (11) (2001) 1829–1840.
[4] I.-S. Lee, C.-N. Whang, K. Choi, M.-S. Choo, Y.-H. Lee, Characterization of iridium film as a stimulating neural electrode, Biomaterials 23 (11) (2002) 2375–2380.
[5] A.M. Cruz, L. Abad, N.M. Carretero, J. Moral-Vico, J. Fraxedas, P. Lozano, G. Subías, V. Padial, M. Carballo, J.E. Collazos-Castro, N. Casañ-Pastor, Iridium oxohydroxide, a significant member in the family of iridium oxides. Stoichiometry, characterization, and implications in bioelectrodes, J. Phys. Chem. C 116 (8) (2012) 5155–5168.
[6] V.M. Tolosa, K.M. Wassum, N.T. Maidment, H.G. Monbouquette, Electrochemically deposited iridium oxide reference electrode integrated with an electroenzymatic glutamate sensor on a multi-electrode arraymicroprobe, Biosens. Bioelectron. 42 (2013) 256–260.
[7] E. Prats-Alfonso, L. Abad, N. Casañ-Pastor, J. Gonzalo-Ruiz, E. Baldrich, Iridium oxide pH sensor for biomedical applications. Case urea–urease in real urine samples, Biosens. Bioelectron. 39 (1) (2013) 163–169.
[8] S. Kakooei, M.C. Ismail, B.A. Wahjoedi, Electrochemical study of iridium oxide coating on stainless steel substrate, Int. J. Electrochem. Sci. 8 (3) (2013).
[9] C. Zhao, H. Yu, Y. Li, X. Li, L. Ding, L. Fan, Electrochemical controlled synthesis and characterization of well-aligned IrO_2 nanotube arrays with enhanced electrocatalytic activity toward oxygen evolution reaction, J. Electroanal. Chem. 688 (0) (2013) 269–274.
[10] I. Jang, I. Hwang, Y. Tak, Attenuated degradation of a PEMFC cathode during fuel starvation by using carbon-supported IrO_2, Electrochim. Acta 90 (0) (2013) 148–156.
[11] L. Badia-Bou, E. Mas-Marza, P. Rodenas, E.M. Barea, F. Fabregat-Santiago, S. Gimenez, E. Peris, J. Bisquert, Water oxidation at hematite photoelectrodes with an iridium-based catalyst, J. Phys. Chem. C 117 (8) (2013) 3826–3833.
[12] Y. Zhao, E.A. Hernandez-Pagan, N.M. Vargas-Barbosa, J.L. Dysart, T. E. Mallouk, A high yield synthesis of ligand-free iridium oxide nanoparticles with high electrocatalytic activity, J. Phys. Chem. Lett. 2 (5) (2011) 402–406.
[13] T. Kuwabara, E. Tomita, S. Sakita, D. Hasegawa, K. Sone, M. Yagi, Characterization and analysis of self-assembly of a highly active colloidal catalyst for water oxidation onto transparent conducting oxide substrates, J. Phys. Chem. C 112 (10) (2008) 3774–3779.
[14] M. Yagi, E. Tomita, S. Sakita, T. Kuwabara, K. Nagai, Self-assembly of active IrO_2 colloid catalyst on an ITO electrode for efficient electrochemical water oxidation, J. Phys. Chem. B 109 (46) (2005) 21489–21491.
[15] S. Fierro, A. Kapałka, C. Comninellis, Electrochemical comparison between IrO_2 prepared by thermal treatment of iridium metal and IrO_2 prepared by thermal decomposition of H_2IrCl_6 solution, Electrochem. Commun. 12 (1) (2010) 172–174.
[16] P.S. Patil, P.S. Chigare, S.B. Sadale, T. Seth, D.P. Amalnerkar, R. K. Kawar, Thickness-dependent properties of sprayed iridium oxide thin films, Mater. Chem. Phys. 80 (3) (2003) 667–675.
[17] R.K. Kawar, P.S. Chigare, P.S. Patil, Substrate temperature dependent structural, optical and electrical properties of spray deposited iridium oxide thin films, Appl. Surf. Sci. 206 (1–4) (2003) 90–101.
[18] S.S. Thanawala, R.J. Baird, D.G. Georgiev, G.W. Auner, Amorphous and crystalline IrO_2 thin films as potential stimulation electrode coatings, Appl. Surf. Sci. 254 (16) (2008) 5164–5169.
[19] C. Pinnow, I. Kasko, N. Nagel, T. Mikolajick, C. Dehm, F. Jahnel, M. Seibt, U. Geyer, K. Samwer, Oxygen tracer diffusion in IrO_2 barrier films, J. Appl. Phys. 91 (3) (2002) 1707–1709.
[20] P. Liao, W. Ho, Y. Huang, K. Tiong, Characterization of sputtered iridium dioxide thin films, J. Mater. Res. 13 (05) (1998) 1318–1326.
[21] Y. Gong, C. Wang, Q. Shen, L. Zhang, Microstructure and properties of annealed IrO_2 thin films prepared by pulsed laser deposition, Mater. Chem. Phys. 116 (2–3) (2009) 573–577.
[22] Y. Zhao, N.M. Vargas-Barbosa, E.A. Hernandez-Pagan, T.E. Mallouk, Anodic deposition of colloidal iridium oxide thin films from hexahydroxyiridate(IV) solutions, Small 7 (14) (2011) 2087–2093.
[23] Y. Kazusuke, Anodically electrodeposited iridium oxide films (AEIROF) from alkaline solutions for electrochromic display devices, Jpn. J. Appl. Phys. 28 (4R) (1989) 632.
[24] W.P. Griffith, The Chemistry of Ruthenium Oxidation Complexes, Ruthenium Oxidation Complexes, Springer, 2011, p. 1–134.
[25] Z. Cheng, J. Xu, H. Zhong, J. Song, A modified electroless route to monodisperse and uniform nickel nanoparticle, Mater. Chem. Phys. 131 (1–2) (2011) 4–7.
[26] C.-M. Chen, C.-H. Chen, S.-J. Cherng, T.-C. Wei, Electroless deposition of platinum on indium tin oxide glass as the counterelectrode for dye-sensitized solar cells, Mater. Chem. Phys. 124 (1) (2010) 173–178.
[27] F. Jamali-Sheini, Chemical solution deposition of ZnO nanostructure films: morphology and substrate angle dependency, Ceram. Int. 38 (5) (2012) 3649–3657.
[28] N. Cai, J. Cho, Low temperature processed SnO_2 films using aqueous precursor solutions, Ceram. Int. 39 (1) (2013) 143–151.
[29] P. Steegstra, E. Ahlberg, Involvement of nanoparticles in the electrodeposition of hydrous iridium oxide films, Electrochim. Acta 68 (2012) 206–213.
[30] T. Ioroi, N. Kitazawa, K. Yasuda, Y. Yamamoto, H. Takenaka, Iridium oxide/platinum electrocatalysts for unitized regenerative polymer electrolyte fuel cells, J. Electrochem. Soc. 147 (6) (2000) 2018–2022.
[31] Z. Yi, C. Kangning, W. Wei, J. Wang, S. Lee, Effect of IrO_2 loading on RuO_2–IrO_2–TiO_2 anodes: a study of microstructure and working life for the chlorine evolution reaction, Ceram. Int. 33 (6) (2007) 1087–1091.
[32] J. Moral-Vico, S. Sánchez-Redondo, M. Lichtenstein, C. Suñol, N. Casañ-Pastor, Nanocomposites of iridium oxide and conducting polymers as electroactive phases in biological media, Acta Biomater. (2014).
[33] R. Green, P. Matteucci, R. Hassarati, B. Giraud, C. Dodds, S. Chen, P. Byrnes-Preston, G. Suaning, L. Poole-Warren, N. Lovell, Performance of conducting polymer electrodes for stimulating neuroprosthetics, J. Neural Eng. 10 (1) (2013) 016009.
[34] Y.L. Pan, T. Noda, K. Sasagawa, T. Tokuda, J. Ohta, Sputtering condition optimization of sputtered IrO_x and TiN stimulus electrodes for retinal prosthesis, IEEJ Trans. Electr. Electron. Eng. 8 (3) (2013) 310–312.
[35] N.D. Schley, J.D. Blakemore, N.K. Subbaiyan, C.D. Incarvito, F. D'Souza, R.H. Crabtree, G.W. Brudvig, Distinguishing homogeneous from heterogeneous catalysis in electrode-driven water oxidation with molecular iridium complexes, J. Am. Chem. Soc. 133 (27) (2011) 10473–10481.
[36] A. Harriman, J. Thomas, G. MILWARD, Catalytic and structural properties of iridium–iridium dioxide colloids, New J. Chem. 11 (11-12) (1987) 757–762.
[37] Y.-C. Hsieh, L.-C. Chang, P.-W. Wu, Y.-M. Chang, J.-F. Lee, Displacement reaction of Pt on carbon-supported Ru nanoparticles in hexachloroplatinic acids, Appl. Catal., B 103 (1) (2011) 116–127.
[38] S.E. Castillo-Blum, D.T. Richens, A.G. Sykes, Oxidation of hexaaquairidium(III) and related studies: preparation and properties of iridium(III), iridium(IV), and iridium(V) dimers as aqua ions, Inorg. Chem. 28 (5) (1989) 954–960.
[39] U. Hintermair, S.M. Hashmi, M. Elimelech, R.H. Crabtree, Particle formation during oxidation catalysis with Cp✻ iridium complexes, J. Am. Chem. Soc. 134 (23) (2012) 9785–9795.
[40] S.E. Castillo-Blum, D.T. Richens, A.G. Sykes, New aqua ions of iridium in oxidation states (III), (IV), and (V),, J. Chem. Soc., Chem. Commun. 14 (1986) 1120–1121.
[41] J.H. Sinfelt, G.D. Meitzner, X-ray absorption edge studies of the electronic structure of metal catalysts, Acc. Chem. Res. 26 (1) (1993) 1–6.
[42] P.-C. Chen, S.-J. Hsieh, C.-C. Chen, J. Zou, Fabrication and characterization of chemically sensitive needle tips with aluminum oxide nanopores for pH indication, Ceram. Int. 39 (3) (2013) 2597–2600.